



**HAL**  
open science

## Revealing the effects of galaxy interaction in the main galaxies of the southern group Arp 314

S. Torres-Flores, P. Amram, D. Olave-Rojas, N. Muñoz-Elgueta, C. Mendes de Oliveira, D. de Mello, F. Urrutia-Viscarra

► **To cite this version:**

S. Torres-Flores, P. Amram, D. Olave-Rojas, N. Muñoz-Elgueta, C. Mendes de Oliveira, et al.. Revealing the effects of galaxy interaction in the main galaxies of the southern group Arp 314. Monthly Notices of the Royal Astronomical Society, 2020, 494, pp.2785-2797. 10.1093/mnras/staa804 . insu-03667100

**HAL Id: insu-03667100**

**<https://insu.hal.science/insu-03667100>**

Submitted on 7 Jul 2023

**HAL** is a multi-disciplinary open access archive for the deposit and dissemination of scientific research documents, whether they are published or not. The documents may come from teaching and research institutions in France or abroad, or from public or private research centers.

L'archive ouverte pluridisciplinaire **HAL**, est destinée au dépôt et à la diffusion de documents scientifiques de niveau recherche, publiés ou non, émanant des établissements d'enseignement et de recherche français ou étrangers, des laboratoires publics ou privés.

# Revealing the effects of galaxy interaction in the main galaxies of the southern group Arp 314

S. Torres-Flores<sup>1</sup>,<sup>1</sup>★ P. Amram,<sup>2</sup> D. Olave-Rojas,<sup>3,4</sup> N. Muñoz-Elgueta,<sup>1</sup>  
C. Mendes de Oliveira,<sup>5</sup> D. de Mello<sup>6</sup> and F. Urrutia-Viscarra<sup>7</sup>

<sup>1</sup>Departamento de Física y Astronomía, Universidad de La Serena, Av. Juan Cisternas 1200 Norte, La Serena, Chile

<sup>2</sup>Aix Marseille Université, CNRS, CNES, LAM (Laboratoire d'Astrophysique de Marseille), Marseille, France

<sup>3</sup>Departamento de Astronomía, Universidad de Concepción, Casilla 160-C, Concepción, Chile

<sup>4</sup>Departamento de Física, Facultad de Ciencias, Universidad del Bío-Bío, Av. Collao 1202, Concepción, Chile

<sup>5</sup>Instituto de Astronomia, Geofísica e Ciências Atmosféricas, Universidade de São Paulo, 05508-090 São Paulo, Brazil

<sup>6</sup>Observational Cosmology Laboratory, Code 665, Goddard Space Flight Center, Greenbelt, MD 20771, USA

<sup>7</sup>Gemini Observatory, Southern Operations Center, c/o AURA, Casilla 603, La Serena, Chile

Accepted 2020 March 12. Received 2020 March 9; in original form 2018 November 30

## ABSTRACT

We present new Gemini imaging and spectroscopic data of the system Arp 314, which consists of a triplet of interacting galaxies. This new imagery exhibits tidal tails and stellar bridges between the galaxies' members and confirms the past interactions. Using this data set, we have analysed the physical properties of 22 star-forming regions located in the main disc of these galaxies, as well as in the intergalactic medium. All these regions have emission lines typical of young ages and a couple of them display very high  $H\alpha$  luminosities ( $L_{H\alpha} \sim 10^{40}$  erg s<sup>-1</sup>). Using the star-forming regions located in Arp 314-1, we derive its gas-phase oxygen-abundance distribution, which suggests a flatter behaviour than the distribution shown by non-interacting systems. This is in agreement with results obtained for other interacting systems and simulations. The presence of gas flows, as indicated by its complex kinematics, could explain this finding. Most of the star formation in Arp 314-2 is located in a central starburst, where double  $H\alpha$  profiles can be identified, as shown by archival Fabry–Perot data. Additionally, we found that the irregular galaxy Arp 314-3 has a low oxygen abundance. Considering its luminosity, this object has a primordial origin, and it was not formed during the interaction event that this system has experienced.

**Key words:** galaxies: abundances – galaxies: interactions – intergalactic medium – galaxies: star clusters: general – galaxies: star formation.

## 1 INTRODUCTION

Small groups of interacting galaxies are prime environments at  $z \sim 0$  to study galaxy evolution, mainly due to their low velocity dispersions ( $\sigma \sim 200$  km s<sup>-1</sup>) and low-galaxy–galaxy separation (typically of the same order of the galaxy diameter), which facilitates interaction and merging of the galaxy members. Given the strong gravitational encounters that may take place in these small interacting groups (triplets, compact groups, and multiplets, in general), one can expect substantial galaxy transformation to happen. Galaxy interactions in dense environments, such as those described above, could trigger nuclear activity, gas flows, metal mixing, formation of new objects and star formation (e.g. Ellison et al. 2008; Ellison et al. 2010; Scudder et al. 2012). However, this

latter effect is very limited, from a statistical point of view (Larson, Tinsley & Caldwell 1980; Ellison et al. 2013, Barrera-Ballesteros et al. 2015; Knapen, Cisternas & Querejeta 2015), which is in agreement with the results derived from simulations (Di Matteo et al. 2007, 2008; Moreno et al. 2015). Moreover, galaxy groups can also play an important role in the pre-processing of galaxies, i.e. galaxies should quench their star formation in groups prior to the infall into the cluster environment (e.g. Zabludoff & Mulchaey 1998; Fujita 2004).

Detailed studies of individual galaxies in small groups can deliver important information regarding the influence of the environment on their physical properties (star formation, nuclear activity, metallicity, etc.). A natural way to carry out these studies is the use of multiobject spectroscopic data. In addition, kinematic data are extremely useful to search for gas inflows and outflows (e.g. Rupke, Veilleux & Sanders 2005; Arribas et al. 2014), which can be associated with metal mixing and nuclear activity. In this sense, a

\* E-mail: [sptorres@userena.cl](mailto:sptorres@userena.cl)

complementary analysis between the physical and kinematical properties of interacting galaxies is a powerful approach to understand these systems and to determine the influence of the environment in the galaxy evolution, specially in the understanding of metal distributions. This motivated us to perform a complete study of the spectacular interacting galaxy group Arp 314, by using optical spectroscopic information and high-resolution kinematic Fabry–Perot data.

The system Arp 314, at a distance of  $51.1 \pm 3.6$  Mpc ( $H_0 = 73.0 \text{ km sec}^{-1} \text{ Mpc}^{-1}$ ; Mould et al. 2000), was classified for the first time by Arp (1966) and it consists of two late-type spiral galaxies (Arp 314-1 and Arp 314-2) and one irregular galaxy (Arp 314-3). The median galaxy separation of this triplet is  $\sim 23$  kpc (considering a scale of  $14.85 \text{ kpc arcmin}^{-1}$ , NED data base). The neutral gas distribution and content of this system was studied by Nordgren et al. (1997), who found a large HI cloud that covers all members. Torres-Flores et al. (2014b) studied the kinematics of the three main galaxies of Arp 314, by using H $\alpha$  Fabry–Perot data cubes. These authors found perturbed velocity fields for members Arp 314-1 and Arp 314-2, which translated into perturbed rotation curves. Although the dwarf galaxy Arp 314-3 is also perturbed, it displays a clear velocity gradient. Arp 314 is therefore an ideal target to investigate environmental effects in galaxies.

This paper is organized as follows. In Sections 2 and 3, we present the data and data analysis. In Section 4, we present the results. In Section 5, we discuss our results, and in Section 6, we summarize our results.

## 2 DATA

### 2.1 Imaging and spectroscopy

We have obtained  $u'$ -,  $g'$ -, and  $r'$ -band imaging and multislit spectroscopic data of Arp 314 by using the Gemini MultiObject Spectrograph (GMOS; Hook et al. 2004) at the Gemini South Observatory, under the programme GS-2013B-Q-27 (PI: S. T-F).

We observed five, four, and three exposures of 300 s each in the filters  $u'$ ,  $g'$ , and  $r'$ , respectively. This allowed the derivation of a false colour image of the main galaxies of this system, as shown in the top panel of Fig. 1. In this image, it is possible to observe the faint stellar structures visible in the intergalactic medium of this system, which mainly corresponds to tidal structures.

In order to design the GMOS spectroscopic mask, we used the false colour image shown in Fig. 1 to select the bluest star-forming regions located across the field, mainly in the disc and tidal structures of our targets. These sources were selected by having optical colours between  $(-0.3 < g'-r < 1.2)$  and  $(-0.3 < u'-g < 1.5)$ , which provide us a useful sample of star-forming regions. We note that this selection criteria has been defined based on our goal of detecting young objects in general and emission-line sources in particular. We observe four exposures of 1370 s each, using the grating R400. Observations were centered at 605, 595, 605, and 600 nm, with a slit width of  $1.0 \text{ arcsec}$  (given that most of our sources are point-like objects). The different central wavelengths were used to remove the gaps in the CCDs. The heights of the slits were changed depending on the source size, and also maximizing the number of objects in the mask design. The position angle of the observations was  $135^\circ$  for Arp 314. In Table 1, we list the coordinates of the slits located in the system Arp 314.

The use of the grating R400 allowed us to observe the main nebular emission lines necessary to determine oxygen abundances (e.g. Marino et al. 2013). The spectral coverage included H $\beta$ ,

[O III] 4959 Å, [O III] 5007 Å, [N II] 6548 Å, H $\alpha$ , and [N II] 6584 Å emission lines for all observed sources. Depending on the position of the mask, for some regions it was also possible to observe H $\gamma$ . CuAr arc lamps were observed after each science observation. Data reduction was performed using the GEMINI reduction package, in IRAF. Having in hand a suitable set of bias and flat fields, each frame was then corrected using the IRAF tasks GBIAS, GFLAT, and GSREDUCE. Wavelength calibrations were done using the GSWAVELENGTH task. Continuum and sky emission lines were removed with the GSSKYSUB task. Finally, flux calibration was done by using the observations of the standard star LTT3218.

### 2.2 Fabry–Perot data

Gas flows have often been invoked as a mechanism to produce a flattening in the metallicity distribution of galaxies, mainly due to metal mixing during galaxy collisions (e.g. Rupke, Kewley & Barnes 2010a). In Section 4.2, we use H $\alpha$  Fabry–Perot data of Arp 314 to search for gas flows in this system. The goal is to combine these results with those derived from the oxygen-abundance analysis (described in Section 4.1), in order to investigate if there is a correspondence between gas flows and flat metallicity distribution for this specific system. Fabry–Perot data of Arp 314 covering the three members of Arp 314, with a spectral resolution of  $R = 12\,600$ , were published in Torres-Flores et al. (2014b).

### 2.3 Complementary data

In order to complement the analysis presented in this paper, we have searched for mid-infrared data of the main galaxies of Arp 314. We searched for data in the *Wide-Field Infrared Survey Explorer* (WISE; Wright et al. 2010) archive and in Table 2, we list the different magnitudes for each galaxy. The values listed in Table 2 correspond to the  $wxgmag$  value listed in the all-sky release source catalogue and these fluxes have been measured in elliptical apertures considering previous 2MASS detections. In the case of the  $wxgmag$  values, the  $x$  corresponds to the different filters available in WISE (W1, W2, W3, and W4). We note that we do not find WISE magnitudes for Arp 314-3. In addition, we have searched for ultraviolet (UV) GALEX data for Arp 314. The UV/GALEX data can trace star formation up to 200 Myr, in comparison with the optical nebular emission associated with H $\alpha$ , which traces current star formation. Arp 314 has been observed by this satellite and the general properties of its galaxies have been published by Muñoz-Mateos et al. (2007) and Gil de Paz et al. (2007).

## 3 ANALYSIS

In this section, we describe the analysis that we have performed on the Gemini/GMOS spectroscopic and ESO/3.60m Fabry–Perot data of Arp 314.

### 3.1 Extinctions and flux measurements

Spectra of star-forming sources have been corrected by Galactic and internal extinctions. We applied the Galactic extinction law suggested by Fitzpatrick (1999), assuming a colour excess of  $E(B-V) = 0.06$  (NED data base). The internal extinction has been derived by comparing the observed and intrinsic Balmer line ratios between H $\alpha$  and H $\beta$ . The observed fluxes of the H $\alpha$  and H $\beta$  emission lines were estimated with the routine PAN, in IDL, which allows us to

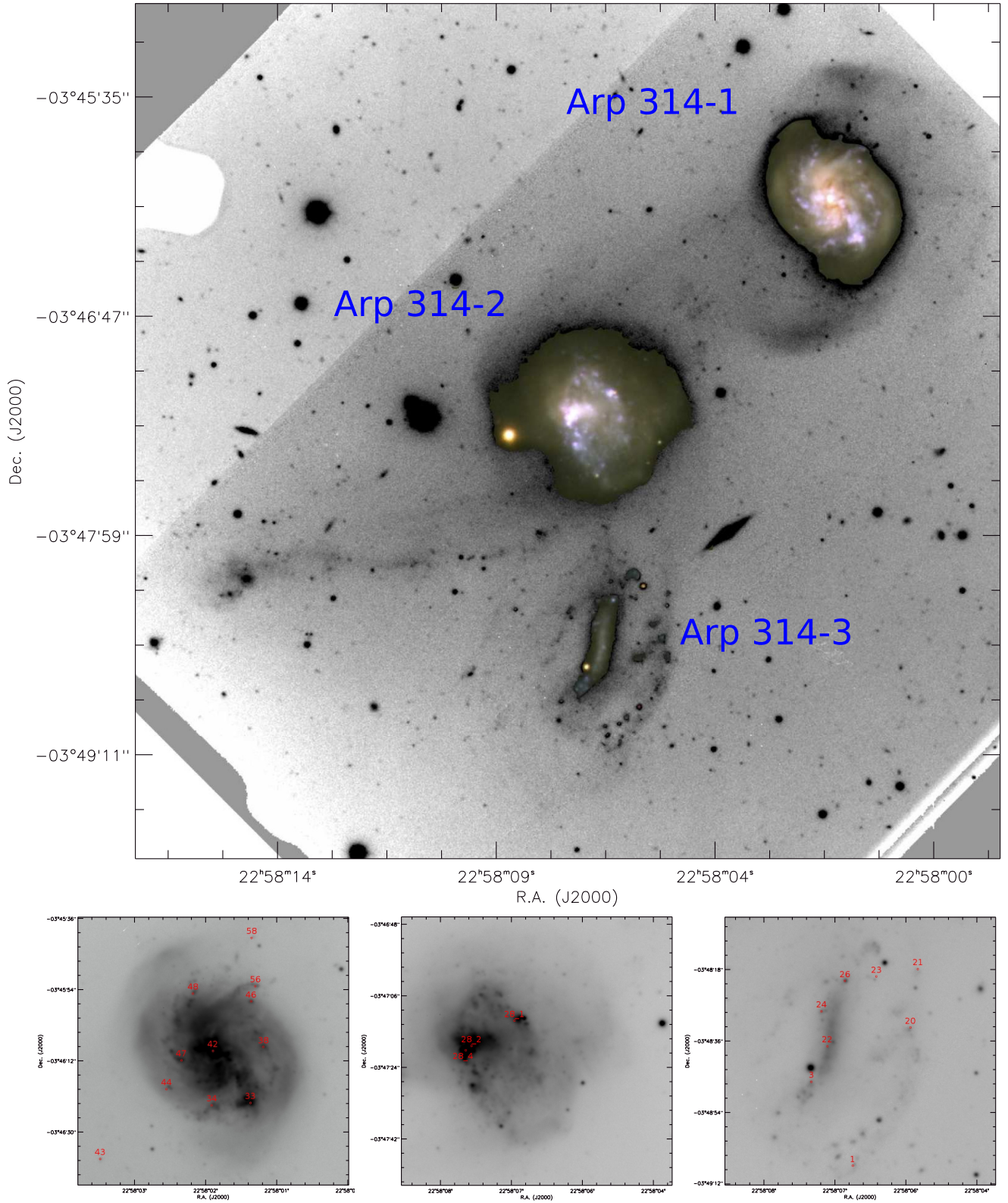


**Figure 1.** Top panel:  $r'$ -band high-contrast image of Arp 314. Tidal structures can be identified on this image. Overplotted,  $u'$ -,  $g'$ -, and  $r'$ -band Gemini/GMOS false colour images of Arp 314-1 and Arp 314-2 are shown, in order to highlight the star-forming regions. Bottom left-hand panel to bottom right-hand panel: Arp 314-1, Arp 314-2, and Arp 314-3  $r'$ -band images. Regions with spectroscopic data are labelled (see Table 1 for coordinates). The  $r'$ -band image has a depth of  $23.7 \text{ [mag arcsec}^{-2}\text{]}$ , which corresponds to the  $3\text{-}\sigma$  limit in a  $10 \times 10 \text{ arcsec}^2$  box.

**Table 1.** Positions, radial velocities, and internal extinctions for sources in Arp 314.

ID	RA (J2000)	Dec. (J2000)	$E(B-V)^1$ (mag)	Velocity <sup>2</sup> (km s <sup>-1</sup> )
(1)	(2)	(3)	(4)	(5)
1	22:58:06.898	-3:49:07.46	0.00	3926 ± 95
3	22:58:07.594	-3:48:46.31	0.15	3835 ± 186
20	22:58:05.926	-3:48:32.65	0.00	3649 ± 185
21	22:58:05.798	-3:48:17.89	0.31	3686 ± 42
22	22:58:07.325	-3:48:37.35	0.06	3845 ± 29
23	22:58:06.499	-3:48:19.81	0.63	3788
24	22:58:07.423	-3:48:28.55	0.08	3785 ± 219
26	22:58:07.030	-3:48:20.90	0.18	3798
33	22:58:01.630	-3:46:22.69	0.22	3699
34	22:58:02.280	-3:46:23.29	0.63	3767
38	22:58:01.411	-3:46:08.63	0.32	3645 ± 25
42	22:58:02.261	-3:46:09.57	...	3685 ± 69
43	22:58:04.162	-3:46:36.80	0.00	3664 ± 124
44	22:58:03.043	-3:46:19.21	0.04	3579 ± 192
46	22:58:01.618	-3:45:57.13	0.05	3787 ± 72
47	22:58:02.794	-3:46:11.97	0.19	3606 ± 71
48	22:58:02.597	-3:45:55.13	0.12	3518 ± 73
56	22:58:01.546	-3:45:53.28	0.09	3735 ± 321
58	22:58:01.608	-3:45:41.10	0.09	3721 ± 58
28_1	22:58:07.147	-3:47:12.27	0.14	3525 ± 46
28_2	22:58:07.874	-3:47:18.62	0.22	3541
28_4	22:58:07.968	-3:47:19.67	0.12	3561

<sup>1</sup>Colour excess of the stellar continuum for each source. These values were estimated following Calzetti et al. (2000). See Section 3.1 for details. <sup>2</sup>Radial velocities measured by using the task EMSAO, in IRAF. See Section 3.1 for details.

**Table 2.** WISE information for galaxies in Arp 314.

ID	3.4 $\mu\text{m}$ (mag)	4.6 $\mu\text{m}$ (mag)	12 $\mu\text{m}$ (mag)	22 $\mu\text{m}$ (mag)
(1)	(2)	(3)	(4)	(5)
Arp 314-1	10.27 ± 0.01	10.07 ± 0.01	5.09 ± 0.01	3.37 ± 0.01
Arp 314-2	10.75 ± 0.01	10.58 ± 0.01	6.96 ± 0.01	4.23 ± 0.03
Arp 314-3	-	-	-	-

fit a single Gaussian on each observed emission-line profile. For the intrinsic Balmer decrement, we assume a value of  $H\alpha/H\beta = 2.86$ , for an electronic temperature of  $T = 10\,000$  K and an electron density of  $N_e = 100\text{ cm}^{-3}$  (Osterbrock 1989). This analysis allows us to obtain a gaseous colour excess  $E(B-V)$  following Domínguez et al. (2013), which was converted into the colour excess of the stellar continuum [ $E_\star(B-V) = 0.44 \times E(B-V)$ ; Calzetti et al. 2000]. This colour excess [ $E_\star(B-V)$ ] was used to correct each spectrum by internal extinction, by using Calzetti et al. (2000)'s extinction law, which was adopted taking into account the star-forming nature of our sources. As an example of the spectroscopic information, in the top and bottom panels of Fig. 2, we show the GMOS optical spectra of two regions belonging to Arp 314-2 and Arp 314-3. On these panels, we have labelled the most important emission lines that were identified in these spectra. Moreover, most of the faint emission lines were not identified in all the spectra available for Arp 314, as can be seen in the bottom panel of this figure. For these reasons, our analysis will be based on the strongest emission lines (i. e.  $H\beta$ , [O III] 4959 Å, [O III] 5007 Å, [N II] 6548 Å,  $H\alpha$  and [N II] 6584 Å).

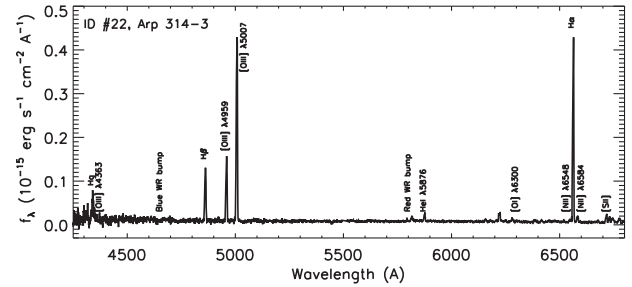
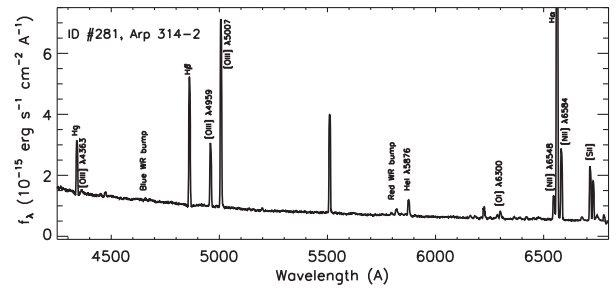


**Figure 2.** Top panel: spectrum of region #28\_1, which corresponds to the brightest  $H\alpha$  source in Arp 314-2. We do not show the entire flux axis, in order to display faint emission features. Bottom panel: spectrum of the most intense star-forming region detected in Arp 314-3. The position of the main emission lines are labelled.

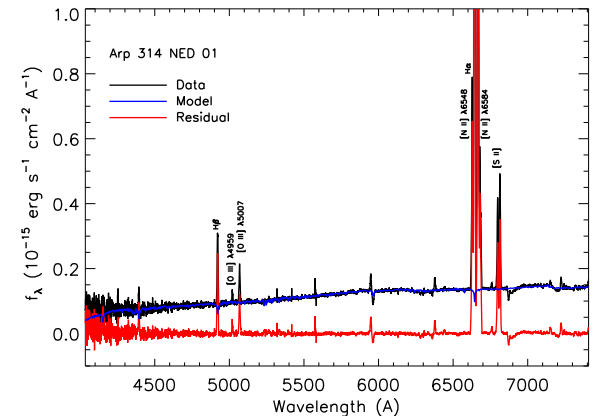


**Figure 3.** Observed spectrum of Arp 314-1 (black curve) and fitted stellar continuum derived from the pPXF analysis (blue curve). The continuum-free spectrum is also displayed (red curve) and the main emission lines are labelled.

In the case of the slits located in the centre of Arp 314-1, the strong stellar continuum emission, which displays absorption features, can affect the measurement of the emission-line fluxes. In order to remove the contribution of the stellar continuum, we have used the penalized pixel-fitting (pPXF) method (Cappellari & Emsellem 2004), which enables us to estimate the stellar continuum emission. We used the MILES stellar library (Sánchez-Blázquez et al. 2006), assuming a Salpeter IMF, 10 ages ranging from 0.063 to 17.78 Gyr, and six metallicities ranging from  $-1.71$  to  $0.22$ . Once the model was derived, we subtracted it from the observed data, in order to obtain a continuum-free spectrum, which was used to measure the line fluxes. The results of this procedure are shown in Fig. 3.

Emission-line fluxes were measured on the extinction-corrected spectra by using the routine SPLIT from IRAF. This routine allows us to fit a single Gaussian on each of the main nebular emission

lines observed in the GMOS data, and also provides uncertainties for the fluxes measurements, which are computed by Monte Carlo simulation. At the end, we measure the fluxes for the main emission lines listed above. Indeed, the physical parameters presented in this paper have been derived from the fluxes listed in Table 3.

We measured the radial velocity for each star-forming region by using the task EMSAO, in IRAF. This routine correlates the observed spectra with a template, which contains information for several emission lines. In the case of six regions (ID #23, #26, #33, #34, #28\_2, and #28\_4), the task EMSAO was not able to determine their radial velocities automatically. In these specific cases, the radial velocity was estimated by using the observed wavelength of the  $H\alpha$  emission line. The task EMSAO does not provide uncertainties in those cases.

### 3.2 Star formation rates (SFRs) and stellar masses

The effect of tidal encounters and mergers can trigger star formation bursts, as found in individual systems like the Antennae galaxies (e.g. Bastian et al. 2009). However, it is worth to note that any enhancement in SFR, from a statistical sense, is very limited (Ellison et al. 2013, and references in Section 1). In order to quantify the effect of the interaction in the galaxies belonging to Arp 314, we have estimated the SFRs for the individual regions and for the galaxies as a whole, by using  $H\alpha$  fluxes and the standard recipe given in Kennicutt (1998) [ $SFR = 7.9 \times 10^{-42} L(H\alpha) \text{ erg s}^{-1}$ ], under the assumption of a continuous star formation process.

SFRs for Arp 314-2 and Arp 314-3 have been computed using three different methods. First, from their  $H\alpha$  fluxes (Fabry–Perot) by using the recipe proposed by Kennicutt (1998). It is important to note that the  $H\alpha$  fluxes published by Torres-Flores et al. (2014b) were not corrected by internal extinction, given that these measurements come from  $H\alpha$  data cubes (Fabry–Perot). Secondly, using the *WISE* data and the calibrations derived for Wen et al. (2014) and Cluver et al. (2014). *WISE* magnitudes were converted into spectral luminosities  $\nu L_\nu$ , considering the corresponding distances. Details about conversion between *WISE* luminosities (e.g. in-band and spectral luminosities) can be found in Jarrett et al. (2013) and Cluver et al. (2014). Thirdly, SFRs were also estimated by using their *GALEX* far-ultraviolet (*FUV*) magnitudes published by Gil de Paz et al. (2007) and Muñoz-Mateos et al. (2007). Magnitudes were corrected by internal extinctions ( $A_{FUV}$ ) and converted into SFRs by using the  $A_{FUV}$  values and calibrations given in Muñoz-Mateos et al. (2007), and considering the distance to each galaxy.

In addition, a number of authors have found that a combination of  $H\alpha$  and mid-infrared (MIR) luminosities can provide a good estimation of the total star formation in a galaxy (e.g. Calzetti et al. 2007; Smith et al. 2007). Wen et al. (2014) provide new calibrations to estimate the total SFRs, by using  $H\alpha$  and MIR *WISE* emission. Then, we have used equation (17) from Wen et al. (2014) to compute the total SFR for Arp 314-2, where the  $H\alpha$  emission comes from the Fabry–Perot data (Torres-Flores et al. 2014b). This estimation is, nevertheless, not valid for Arp 314-1, given its possible active galactic nucleus (AGN) nature, and is not feasible for Arp 314-3, because no *WISE* magnitudes are available.

One of the major difficulties to estimate stellar masses by using luminosity is the assumption of a mass-to-light (M/L) ratio. In this sense, several authors (e.g. Bell & de Jong 2001; Cluver et al. 2014; Meidt et al. 2014) have derived calibrations to estimate this parameter using different methods and luminosities observed in different wavelengths. It is well established that optical/near-infrared luminosities are affected by dust extinction (Cardelli,

Clayton & Mathis 1989). This fact adds another difficulty to the estimation of stellar masses, because we need to adopt a dust model and an extinction law to correct the observations. For this reason, stellar masses for galaxies can be better estimated by using their MIR luminosities, given that these wavelengths are less affected by extinction and they trace the bulk of the stellar emission (e.g. Cluver et al. 2014; Meidt et al. 2014; Querejeta et al. 2015). In addition, Meidt et al. (2014) by using the 3.6- $\mu\text{m}$  emission of a sample of nearby galaxies taken from the Spitzer Survey of Stellar Structure in Galaxies (Muñoz-Mateos et al. 2015) performed precise calibrations for M/L, finding that the M/L ratio estimated by using MIR luminosities is less affected by age, star formation history and metallicity. In our case, and given the current available data, we have used the *WISE* W1 fluxes (3.4  $\mu\text{m}$ ) to estimate the stellar masses of our targets. In order to derive the masses, we have used the calibration proposed by Cluver et al. (2014, equation 1), which involves the use of the colour (W1–W2) and the W1 luminosity.

### 3.3 Gas-phase oxygen abundances

For all sources observed in Arp 314, except for ID#28\_1, it was not possible to measure the [O III] 4363 $\lambda$  line (we detect a weak contribution of the [O III] 4363 $\lambda$  emission line in the region ID#28\_1, see top panel of Fig. 2). For this reason, we have used the O3N2 method and thus, the prescription given by Marino et al. (2013) (see also Pettini & Pagel 2004) to determine oxygen abundances. It is worth noting that the empirical calibration methods display large uncertainties ( $\sim 0.2$  dex), which are associated with the proper scatter of the calibrator. Also, the use of different methods can give us different estimates for the oxygen abundances. However, when a single calibrator is used for a given sample, we can have a reliable determination of the metallicity distribution (see Scarano, Lépine & Marcon-Uchida 2011; Bresolin, Kennicutt & Ryan-Weber 2012). This is important for this kind of studies, where metallicity distributions are analysed. In this context, our final measurements include the uncertainties of 0.2 dex derived from the scatter of the calibrators, however, the actual uncertainties arises from the flux estimates.

## 4 RESULTS

In the following section, we describe the main results of this work, emphasizing oxygen distributions and kinematical results for Arp 314.

### 4.1 Gas-phase oxygen abundances

#### 4.1.1 Diluted metallicities in Arp 314

In the case of the star-forming complexes observed in Arp 314-1 and Arp 314-2, we measured oxygen abundances  $12 + \log(O/H)$  that range from 8.24 to 8.49. All these oxygen abundances are sub-solar [considering a solar oxygen abundance of  $12 + \log(O/H)_\odot = 8.72$ ; Allende Prieto, Lambert & Asplund 2001]. Considering the *B*-band absolute magnitude of Arp 314-1 and Arp 314-2, which corresponds to  $M_B = -20.62$  and  $M_B = -20.28$ , respectively (HyperLeda data base), we found that both galaxies lie off the *B*-band metallicity–luminosity relation studied by Kewley, Geller & Barton (2006), i.e. these galaxies display lower abundances for their luminosities or high luminosities for their abundances. However, we note that the *B*-band luminosity of these galaxies should be affected by the star formation episodes that are taking place in these galaxies. In order to

**Table 3.** Line fluxes for the star-forming regions located in the tidal tail and main body of Arp 314.

ID	H $\beta$	[O III] $\lambda$ 4959	[O III] $\lambda$ 5007 ( $10^{-15}$ erg cm $^{-2}$ s $^{-1}$ Å $^{-1}$ )	[N II] $\lambda$ 6548	H $\alpha$	[N II] $\lambda$ 6584	12 + log(O/H)	$L_{\text{H}\alpha}$ (erg s $^{-1}$ )	SFR ( $M_{\odot}$ yr $^{-1}$ )
(1)	(2)	(3)	(4)	(5)	(6)	(7)	(8)	(9)	(10)
1	0.11 ± 0.07	0.17 ± 0.01	0.33 ± 0.01	0.01 ± 0.01	0.23 ± 0.01	0.01 ± 0.01	8.12 ± 0.22	10 <sup>37.85</sup> ± 10 <sup>36.91</sup>	0.001 ± 0.001
3	0.32 ± 0.02	0.39 ± 0.02	0.86 ± 0.01	0.02 ± 0.01	0.64 ± 0.01	0.01 ± 0.01	<8.1	10 <sup>38.30</sup> ± 10 <sup>37.24</sup>	0.002 ± 0.001
20	0.24 ± 0.01	0.19 ± 0.01	0.40 ± 0.01	0.02 ± 0.01	0.25 ± 0.01	0.01 ± 0.01	8.11 ± 0.21	10 <sup>37.90</sup> ± 10 <sup>36.94</sup>	0.001 ± 0.001
21	0.20 ± 0.03	0.02 ± 0.01	0.45 ± 0.03	0.00 ± 0.00	0.58 ± 0.03	0.02 ± 0.01	8.13 ± 0.20	10 <sup>38.26</sup> ± 10 <sup>37.35</sup>	0.001 ± 0.001
22	0.88 ± 0.01	1.04 ± 0.01	2.92 ± 0.01	0.03 ± 0.01	2.36 ± 0.01	0.11 ± 0.01	8.14 ± 0.18	10 <sup>38.87</sup> ± 10 <sup>37.74</sup>	0.006 ± 0.001
23	0.45 ± 0.06	0.32 ± 0.04	2.62 ± 0.08	0.03 ± 0.05	2.12 ± 0.07	0.02 ± 0.02	<8.1	10 <sup>38.82</sup> ± 10 <sup>37.84</sup>	0.005 ± 0.001
24	0.26 ± 0.01	0.09 ± 0.01	0.17 ± 0.01	0.00 ± 0.00	0.61 ± 0.01	0.06 ± 0.01	8.35 ± 0.18	10 <sup>38.28</sup> ± 10 <sup>37.22</sup>	0.002 ± 0.001
26	2.23 ± 0.02	3.75 ± 0.01	10.65 ± 0.02	0.09 ± 0.03	6.95 ± 0.02	0.24 ± 0.02	<8.1	10 <sup>39.34</sup> ± 10 <sup>38.20</sup>	0.017 ± 0.001
33	6.67 ± 0.07	1.41 ± 0.06	4.17 ± 0.06	2.24 ± 0.06	24.21 ± 0.06	6.83 ± 0.06	8.46 ± 0.18	10 <sup>39.88</sup> ± 10 <sup>38.74</sup>	0.060 ± 0.004
34	0.64 ± 0.21	0.11 ± 0.04	1.07 ± 0.12	0.54 ± 0.09	5.08 ± 0.07	1.30 ± 0.08	8.36 ± 0.18	10 <sup>39.20</sup> ± 10 <sup>38.13</sup>	0.013 ± 0.001
38	0.71 ± 0.07	0.19 ± 0.03	0.78 ± 0.03	0.30 ± 0.05	3.08 ± 0.04	1.03 ± 0.05	8.42 ± 0.18	10 <sup>38.98</sup> ± 10 <sup>37.90</sup>	0.008 ± 0.001
42	22.83 ± 0.24	2.95 ± 0.27	10.63 ± 0.24	28.72 ± 0.22	132.06 ± 0.23	93.73 ± 0.39	–	10 <sup>40.62</sup> ± 10 <sup>39.47</sup>	–
43	0.22 ± 0.01	0.25 ± 0.01	0.57 ± 0.01	0.01 ± 0.00	0.35 ± 0.01	0.04 ± 0.01	8.24 ± 0.18	10 <sup>38.04</sup> ± 10 <sup>37.03</sup>	0.001 ± 0.001
44	0.53 ± 0.01	0.18 ± 0.01	0.47 ± 0.01	0.22 ± 0.01	1.38 ± 0.01	0.40 ± 0.01	8.43 ± 0.18	10 <sup>38.63</sup> ± 10 <sup>37.53</sup>	0.003 ± 0.001
46	0.76 ± 0.01	0.18 ± 0.01	0.39 ± 0.01	0.26 ± 0.01	2.22 ± 0.01	0.75 ± 0.01	8.49 ± 0.18	10 <sup>38.84</sup> ± 10 <sup>37.72</sup>	0.005 ± 0.001
47	1.86 ± 0.02	0.88 ± 0.03	2.21 ± 0.03	0.50 ± 0.03	5.98 ± 0.03	1.44 ± 0.03	8.38 ± 0.18	10 <sup>39.27</sup> ± 10 <sup>38.15</sup>	0.015 ± 0.001
48	0.22 ± 0.02	0.13 ± 0.01	0.51 ± 0.01	0.10 ± 0.01	1.16 ± 0.01	0.28 ± 0.01	8.32 ± 0.18	10 <sup>38.56</sup> ± 10 <sup>37.46</sup>	0.003 ± 0.001
56	0.53 ± 0.01	0.15 ± 0.01	0.39 ± 0.01	0.17 ± 0.02	1.42 ± 0.02	0.44 ± 0.01	8.45 ± 0.18	10 <sup>38.65</sup> ± 10 <sup>37.57</sup>	0.004 ± 0.001
58	0.14 ± 0.01	0.03 ± 0.01	0.30 ± 0.01	0.03 ± 0.01	0.45 ± 0.01	0.12 ± 0.01	8.34 ± 0.18	10 <sup>38.15</sup> ± 10 <sup>37.11</sup>	0.001 ± 0.001
28_1	33.91 ± 0.04	17.13 ± 0.05	48.07 ± 0.05	6.30 ± 0.04	112.52 ± 0.04	18.95 ± 0.04	8.34 ± 0.18	10 <sup>40.55</sup> ± 10 <sup>39.40</sup>	0.278 ± 0.020
28_2	3.46 ± 0.03	1.85 ± 0.03	5.29 ± 0.03	0.86 ± 0.04	8.92 ± 0.03	2.37 ± 0.03	8.37 ± 0.18	10 <sup>39.44</sup> ± 10 <sup>38.31</sup>	0.022 ± 0.002
28_4	10.67 ± 0.03	6.02 ± 0.03	17.42 ± 0.03	2.29 ± 0.04	33.42 ± 0.03	4.80 ± 0.03	8.31 ± 0.18	10 <sup>40.02</sup> ± 10 <sup>38.87</sup>	0.082 ± 0.006

**Table 4.** SFRs, stellar masses and specific SFRs.

ID	SFR <sub>FUV</sub> (M <sub>⊙</sub> yr <sup>-1</sup> )	SFR <sub>Hα</sub> (M <sub>⊙</sub> yr <sup>-1</sup> )	SFR <sub>22μm</sub> (M <sub>⊙</sub> yr <sup>-1</sup> )	SFR <sub>Hα + 22μm</sub> (M <sub>⊙</sub> yr <sup>-1</sup> )	log(M <sub>★</sub> )	log(SFR <sub>Hα + 22μm</sub> /M <sub>★</sub> )
(1)	(2)	(3)	(4)	(5)	(6)	(7)
Arp 314-1	–	–	–	–	9.94	–
Arp 314-2	1.1	1.3	1.9/1.8	2.1	9.81	–9.48
Arp 314-3	–	0.2	–	–	–	–

check it, we have used the stellar mass of these galaxies to determine their location in the mass–metallicity relation studied by Tremonti et al. (2004). Using the masses listed in Table 4 (column 6), we found that Arp 314-1 and Arp 314-2 display slightly lower oxygen abundances for their respective stellar masses. A similar scenario has been found in different interacting systems. In fact, Kewley et al. (2006) suggest that gas inflows dilute the central metallicities of interacting galaxies. More recently, Olave-Rojas et al. (2015) suggest that this mechanism is producing the observed metallicity gradient in NGC 6845A, galaxy that belongs to the group NGC 6845.

In the case of Arp 314-3, three of their star-forming regions display O3N2 values larger than the valid limits given by Marino et al. (2013). This implies that these regions belonging to Arp 314-3 have oxygen abundances lower than  $12 + \log(\text{O}/\text{H})_{\odot} = 8.10$ . In addition, we did not find *WISE* information for this galaxy therefore its mass was not computed. In view of these results, we cannot locate this object in the mass–metallicity relation. However, some speculations can be done regarding its origin. Arp 314-3 displays a Large Magellanic Cloud (LMC)-like morphology, it could be a pristine irregular dwarf or a tidal dwarf galaxy (TDG). If Arp 314-3 was formed from pre-enriched material belonging to Arp314-1 or/and –2, it should show an oxygen abundance similar to these two galaxies. The oxygen abundance of Arp 314-3 measured with the O3N2 index indicates a metallicity of  $12 + \log(\text{O}/\text{H}) = 8.14$ , which is lower than that of Arp 314-1 and Arp 314-2, respectively  $12 + \log(\text{O}/\text{H}) = 8.39$  and  $12 + \log(\text{O}/\text{H}) = 8.34$ . This suggests that Arp 314-3 is a primordial dwarf irregular and not a TDG formed from the interaction of the two main galaxies of the group. This scenario is also supported by the metallicity–luminosity relation studied by Weillbacher, Duc & Fritze-v. Alvensleben (2003), who included in their analysis a sample of TDG candidates. Indeed, considering its *B*-band absolute magnitude,  $M_B = -14.89$  (HyperLeda data base), Arp 314-3 does not lie in the locus of the TDGs.

#### 4.1.2 Flat metal distribution in interacting systems

Using the measured oxygen abundances, we have derived the oxygen-abundance distribution for the galaxy Arp 314-1, which is shown in Fig. 4. Distances have been de-projected by using the kinematical inclination and position angle published in Torres-Flores et al. (2014b), and using the procedure developed by Scarano et al. (2008). On this figure, the solid line represents a linear fit on the data, where we have excluded the nuclear region (region #42), given the contribution of a possible AGN. On the same plot, we have included the oxygen abundances of regions belonging to Arp 314-2 (empty circles). In this latter case, distances correspond to linear projected distances estimated from the centre of Arp 314-1 to each source. Regions belonging to Arp 314-2 were not included in the fit shown. From the linear fit, we derive a zero-point of  $\alpha = 8.48 \pm 0.04$  and a slope of  $\beta = -0.02 \pm 0.01 \text{ dex kpc}^{-1}$ , which is shallower than the slope displayed by the non-interacting galaxies

(e.g.  $\beta = -0.07 \pm 0.01 \text{ dex kpc}^{-1}$ , Zaritsky, Kennicutt & Huchra 1994). Inspecting Fig. 4, we note that most of the star-forming regions for which we measure oxygen abundances are located at radius  $R < 5 \text{ kpc}$ . These star-forming objects do not display a clear oxygen abundance gradient. Indeed, the reported gradient arises when we include regions #58 and # 43 in the fit. These objects are located in the outskirts of Arp 314-1, and are therefore expected to have lower oxygen abundances.

It is important to note that galaxy Arp 314-3 displays a low oxygen abundance, consistent with its luminosity. Nordgren et al. (1997) published the H I distribution of Arp 314 showing a large cloud of H I covering the three main galaxies. If gas-flows or gas-mixing is responsible for the flattening of metallicity gradients in interacting systems, it is puzzling that metals have not mixed yet.

#### 4.2 Kinematics: searching for gas motions

The kinematics of the members of Arp 314 have been already analysed by Torres-Flores et al. (2014b), however, no detailed analyses of the non-circular motions and on the multiple H $\alpha$  emission components have been done. We will use this information, combined with the Gemini spectroscopic data, to understand the observed metal distribution of Arp 314. In Figs 5–7, we show the main kinematic features of Arp 314-1, Arp 314-2, and Arp 314-3, respectively. In panel (a), we show the *r*-band optical image; on panel (b), we show the observed and modelled velocity field (represented by colour bins and a colour map/black lines, respectively); in panel (c), we show the residual velocity field, which corresponds to the difference between the observed and modelled field; in panel (d), we show the central region of the velocity field of each galaxy, where we have superimposed the H $\alpha$  profiles associated with that region. On this panel, each profile represents a  $4 \times 4$  pixels. Countours in panels (b) and (c) represent the H $\alpha$  emission. In the case of panel (b), the modelled velocity fields were derived to obtain the rotation curve of the different galaxies (see Epinat, Amram & Marcelin 2008; Torres-Flores et al. 2014b). The velocity fields and the residual-velocity fields clearly indicate that the three galaxies are far from being pure rotating discs, and in the following, we describe the main kinematic features of each galaxy, which are used to identify gas motions.

In the case of the Sbc galaxy Arp 314-1, Torres-Flores et al. (2014b) reported a relatively regular velocity field. However, they found a misalignment between the morphological and kinematic position angle ( $33^\circ$  and  $115^\circ$ , respectively), which is a typical signature of galaxy interaction. Despite the fact that the galaxy is globally rotating, when we compare the model and the observed velocity fields [Fig. 5, panel ‘(b)’], we observe strong local velocity jumps (for instance, in the outskirts regions of the disc, where the observed field show larger velocity amplitude than the model). These strong kinematical perturbations are clearly visible on the residual-velocity field [Fig. 5, panel ‘(c)’] that shows non-circular motions randomly distributed in the disc, ranging between  $-25$

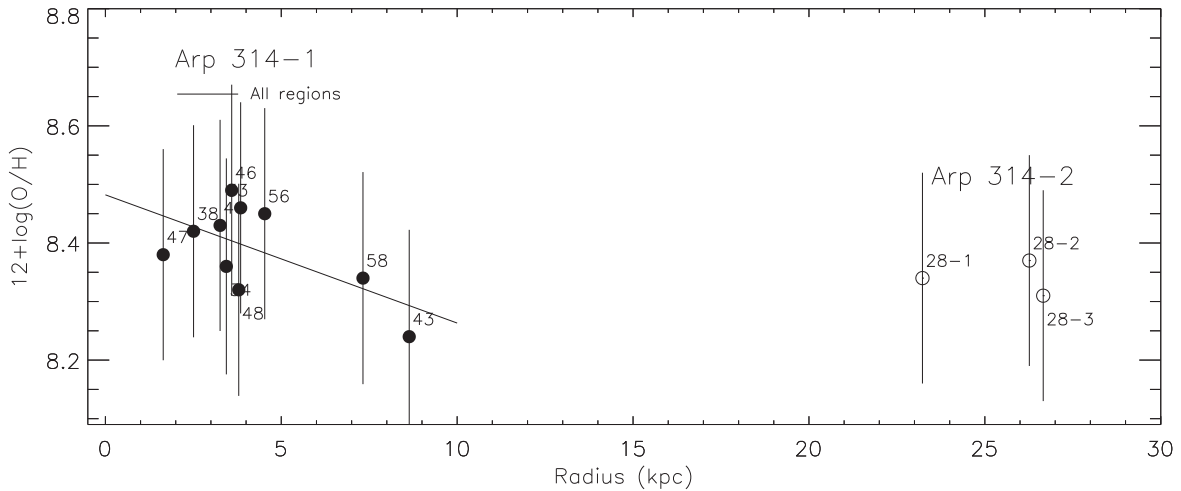


**Figure 4.** Oxygen abundance gradient for Arp 314-1, where different regions are shown by filled black circles. A linear fit on the data is indicated by a black line. Regions belonging to Arp 314-2 are included on the plot (empty circles), in order to show the differences in the oxygen abundances.

to  $+25 \text{ km s}^{-1}$ . These kinds of features can contain rich information related with the interaction history of the galaxies, specially in closely face-on systems. Inspecting the  $\text{H}\alpha$  profiles of Arp 314-1, we mostly found a strong emission line very often accompanied by a second component, which is fainter in intensity. The fainter emission line is either resolved or embedded in an asymmetric profile dominated by the brighter emission line. This may suggest that Arp 314-1 has experienced a recent gas accretion, as has been reported in other interacting systems (e.g. Font et al. 2011). In addition, the slope of the metallicity gradient observed in Arp 314-1 ( $\beta = -0.02 \pm 0.01 \text{ dex kpc}^{-1}$ ) is consistent with the slope measured for a sample of galaxy pairs (Kewley et al. 2010). Kewley et al. (2010) suggest that the flattening in the metal distribution of galaxy pairs should be connected with large gas inflows. Given the modest intensity of the second component versus the main one, the gas flow we observe by inspecting the  $\text{H}\alpha$  profiles of Arp 314-1 is probably not carrying out large quantities of material. If gas inflows were the main mechanism in producing a flattening in the metal distribution of Arp 314-1, these inflows should have already occurred and we would then expect that, presently, the process has already finished or it is at its final phase.

The scenario is even more complicated for the SBc galaxy Arp 314-2. The external region of this galaxy displays a complex velocity field, which does not actually show a well-behaved rotating disc [see Fig. 6, panels (b) and (c)]. The dip in the blueshifted and the bump in the redshifted inner rotation curve (Torres-Flores et al. 2014b), likely due to the strong bar, provide a peculiar pattern for the central isovelocities overplotted on top of the observed velocity field, which does not follow a symmetric rotating disc pattern. Indeed, if we observe a continuity between the data and the model on the blueshifted side of the galaxy, this is not the case on the redshifted side. This can be seen on the very asymmetric residual velocity field showing a blueshift side almost flat [see Fig. 6, panel (c)], but a redshifted side with velocities that jump from  $-50$  to  $+50 \text{ km s}^{-1}$  within a couple of kpc. In fact, these velocities display a ring-like structure. The  $\text{H}\alpha$  profiles of the central region of this galaxy display asymmetric profiles [Fig. 6, panel (d)]. This suggests that more than one kinematic component is present in this region, resulting in broad  $\text{H}\alpha$  emission-line profiles. Towards the northern region of the nucleus of Arp 314-2, we even detect

double  $\text{H}\alpha$  profiles [as can be seen in Fig. 6, panel (d)]. Given the complex kinematic of this system, it is difficult to determine if these double-component profiles arise from a gas inflow. In any case, this galaxy displays an  $\text{SFR}(\text{H}\alpha) \sim 1.1 \text{ M}_{\odot} \text{ yr}^{-1}$ , which suggests that no external gas accretion is dramatically increasing its SFR. However, the central region of this galaxy, where the  $\text{H}\alpha$  emission peaks (inner  $5 \times 5 \text{ arcsec}^2$  centred in RA: 22:58:07.94, Dec: -3:47:19.10), displays velocity dispersions of  $\sim 40 \text{ km s}^{-1}$ . Those values are larger than the typical values for the velocity dispersion displayed by the non-interacting systems ( $\sim 25 \text{ km s}^{-1}$ ; Epinat et al. 2010, for the GHASP survey). Given that there is a spatial correlation between the maximum of the  $\text{H}\alpha$  emission and the maximum velocity dispersion in the central region of Arp 314-2, we cannot exclude that the stellar feedback produced by star formation is increasing the interstellar medium velocity dispersion.

Finally, the kinematic of the irregular SBd dwarf galaxy Arp 314-3 displays, despite its bar, a fairly symmetric rotation disc pattern (Torres-Flores et al. 2014b) of low maximum rotation velocity  $\sim 40 \text{ km s}^{-1}$  at the optical radius and growing up to  $\sim 60 \text{ km s}^{-1}$  at two optical radii. These authors suggest that this object could be an irregular star-forming galaxy or an object formed from tidal debris. The low observed oxygen abundances confirms the first scenario: Arp 314-3 is a primordial irregular galaxy, as discussed in session 4.1.1.

### 4.3 Inspecting the optical morphology of galaxies in Arp 314

Using the Gemini optical imaging data, we have inspected the morphology of each galaxy belonging to Arp 314 (see Fig. 1). We describe, hereafter, the main morphological features of the interacting system, from an optical point of view.

Galaxy Arp 314-1 displays a spiral-arm structure with several bright blue knots clearly associated with star-forming regions. The nucleus is dominated by a strong point-like emission. The outskirts of the galaxy display a diffuse stellar emission in the shape of a shell-like structure. Given their proximity ( $\sim 39 \text{ arcsec}$  from the Arp 314-1 centre), these shells should be formed by an interaction of Arp 314-1 with Arp 314-2 as seen in simulations of interacting galaxies. For instance, Hernquist & Quinn (1989) suggested that shell structures can be formed during the interaction of a low-mass

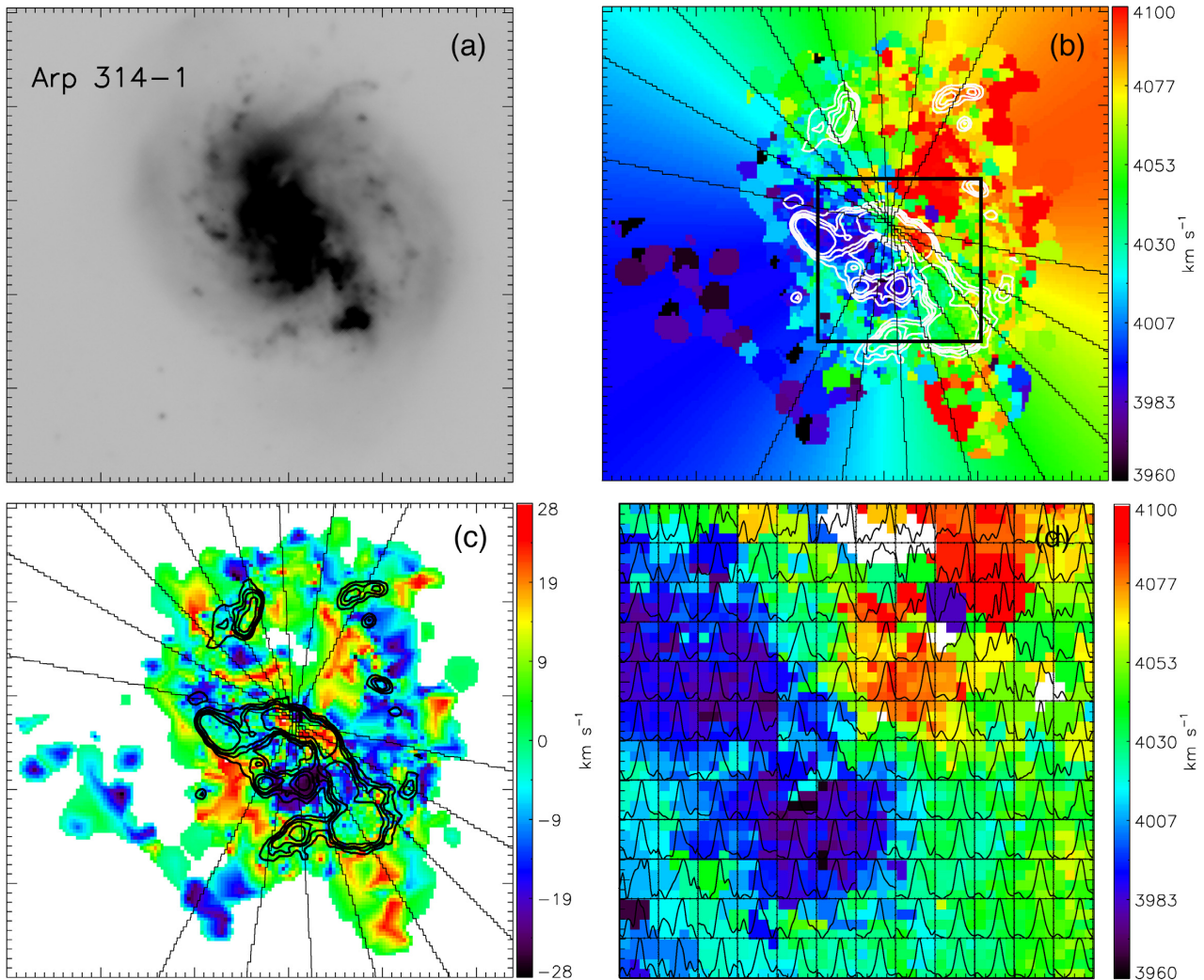


**Figure 5.** Images and velocity fields for Arp 314-1. Panel (a): Gemini  $r$ -band image. Panel (b): observed velocity field on which a kinematic model has been overlotted (which was obtained by Torres-Flores et al. 2014b to derive rotation curves). Black iso-velocities represent the kinematic model and white contours represent  $H\alpha$  emission. Black square represents a region that is amplified in panel (d). Panel c: residual-velocity fields, i.e. difference between the observed and modelled velocity fields, as shown in panel (b). Panel d: zoom-in of the black square shown in panel (b). Normalized  $H\alpha$  profiles have been overlotted (using a bin  $4 \times 4$  pixels).

disc galaxy with a more massive disc galaxy. Galaxy Arp 314-2 displays an extremely perturbed morphology (see Fig. 1), with no spiral pattern being detected and it is observed that a tidal arm that emerges from the south-east side of the galaxy also emerges in this case. Several star-forming regions can be observed across the main body of this object. In particular, we observe three bright knots near its centre, with a diffuse stellar emission to the north-west side of these regions. The region 28\_1 is located at  $\sim 14$  arcsec from the Arp314-2 centre, while the regions 28\_2 and 28\_3 are located at  $\sim 1$  arcsec from the Arp314-2 centre. On the south-east side of Arp 314-2, there is an extended optical tidal tail containing a number of compact knots. Besides that, we observe a diffuse and faint stellar emission between Arp 314-1 and Arp 314-2, which contains a chain of compact sources and seems to connect both galaxies. Finally, Arp 314-3 displays an irregular shape. Its morphology reveals the presence of a stellar bar surrounded by more than a dozen star-forming regions. The morphology of this galaxy resembles that of the LMC.

#### 4.4 Internal extinctions, radial velocities and line fluxes

In the fourth column of Table 1, we list colour excesses estimated as described in Section 3, with the exception of the central spectrum of Arp314-1, given its possible AGN nature. The values of colour excess span from  $E(B-V)_* \sim 0$  to  $E(B-V)_* \sim 0.63$  (the latter value corresponds to  $\sim 2.0$  mag in the  $V$ -band, considering  $R_V = 3.1$ ). These values are consistent with the estimates derived for star-forming regions located in other interacting systems. In the last column of Table 1, we list the radial velocities derived for each region, confirming their membership to their parent galaxies.

In Table 3, we list the flux of the  $H\beta$ ,  $[O III] 4959 \text{ \AA}$ ,  $[O III] 5007 \text{ \AA}$ ,  $[N II] 6548 \text{ \AA}$ ,  $H\alpha$ , and  $[N II] 6584 \text{ \AA}$  emission lines for the different star-forming regions observed in Arp 314, where the most intense sources are associated with the nucleus of Arp 314-1 and with a strong star-forming object, which corresponds to the region 28\_1 which has a  $SFR \sim 0.2 M_\odot \text{ yr}^{-1}$ , which is located at 14 arcsec from the centre of Arp 314-2.

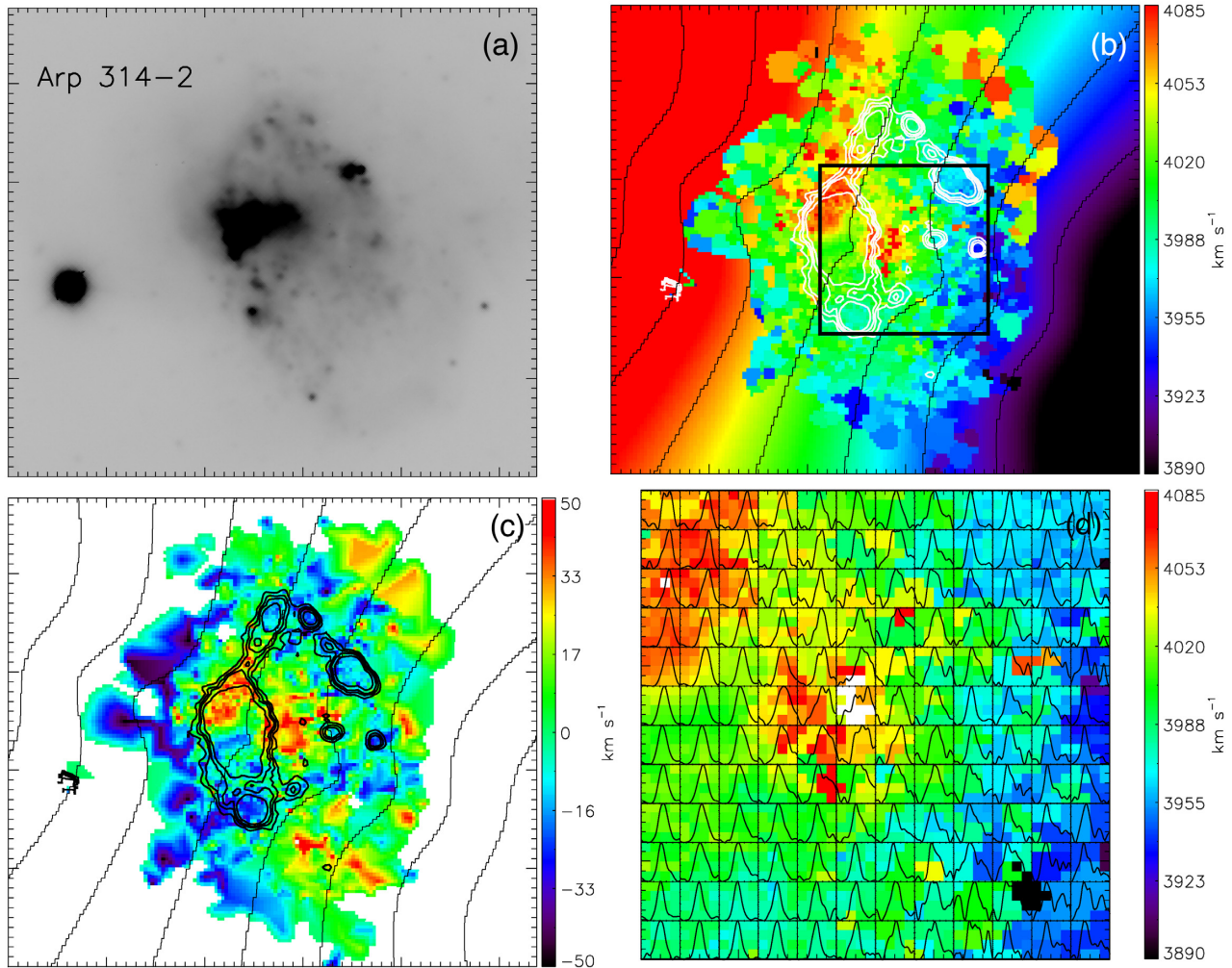


**Figure 6.** Same caption as for Fig. 5, but for Arp 314-2.

## 4.5 SFRs

### 4.5.1 $H\alpha$ luminosities

Considering the distance to Arp 314, we have derived the dust-corrected  $H\alpha$  luminosities for the star-forming complexes (Table 3, column 9). In the case of Arp 314-2, the central regions #28\_1 and #28\_4 display  $H\alpha$  luminosities larger than  $L_{H\alpha} > 10^{40}$  erg  $s^{-1}$ . In addition, region #33 also displays high  $H\alpha$  luminosity, with a  $\log(L_{H\alpha})$  almost equal to  $10^{40}$  erg  $s^{-1}$ . We have located these sources on the dispersion velocity map of Arp 314 published by Torres-Flores et al. (2014b) and we found that these objects display velocity dispersion of  $\sigma \sim 35\text{--}40$  km  $s^{-1}$ . Similar values have been measured for several giant H II regions (GH II R) located in other nearby galaxies (e.g. Kennicutt & Hodge 1984; Hodge 1993; Melnick, Tenorio-Tagle & Terlevich 1999; Hägele et al. 2007; Firpo et al. 2010), suggesting that these star-forming regions detected in Arp 314 are GH II R candidates.

### 4.5.2 Individual star-forming regions

In the last column of Table 3, we list the  $SFR(H\alpha)$  for each individual source observed in Arp 314, under the assumption of a continuous star formation process. In general, individual regions display modest

level of ongoing star formation. A few exceptions can be found in Arp 314-2. For instance, region #28\_1, displays a relatively high  $SFR \sim 0.28 M_{\odot} \text{ yr}^{-1}$ . This region corresponds to an ongoing high-SFR event located outside the nuclear region of this galaxy. On the other hand, regions #1, #3, and #43 display the lower values for the SFRs ( $\sim 10^{-3} M_{\odot} \text{ yr}^{-1}$ ). The case of region #43 is peculiar. This source is located in the bridge that connects Arp 314-1 with Arp 314-2, as can be seen in Fig. 8, suggesting that this source was formed from gaseous material that was ejected during the interaction process.

### 4.5.3 Global estimates: UV, $H\alpha$ , and MIR data

In Table 4, we list the SFRs estimated from the UV,  $H\alpha$ , MIR and  $H\alpha$  corrected by MIR emission for the main galaxies of Arp 314. Indeed, in the case of Arp 314-1, no computation was performed given its possible AGN nature.

The galaxy Arp 314-2 displays  $SFR_{FUV} = 1.1 M_{\odot} \text{ yr}^{-1}$ ,  $SFR(H\alpha) = 1.3 M_{\odot} \text{ yr}^{-1}$ ,  $SFR_{22\mu\text{m}} = 1.9 M_{\odot} \text{ yr}^{-1}$ , and  $SFR_{H\alpha_{\text{obs}}+22\mu\text{m}} = 2.1 M_{\odot} \text{ yr}^{-1}$ .

In the case of Arp 314-3, we just compute the SFR using the  $H\alpha$  emission, obtaining a value of  $SFR(H\alpha) = 0.2 M_{\odot} \text{ yr}^{-1}$  (no  $FUV$  magnitude was found in the *GALEX* archive for this galaxy).

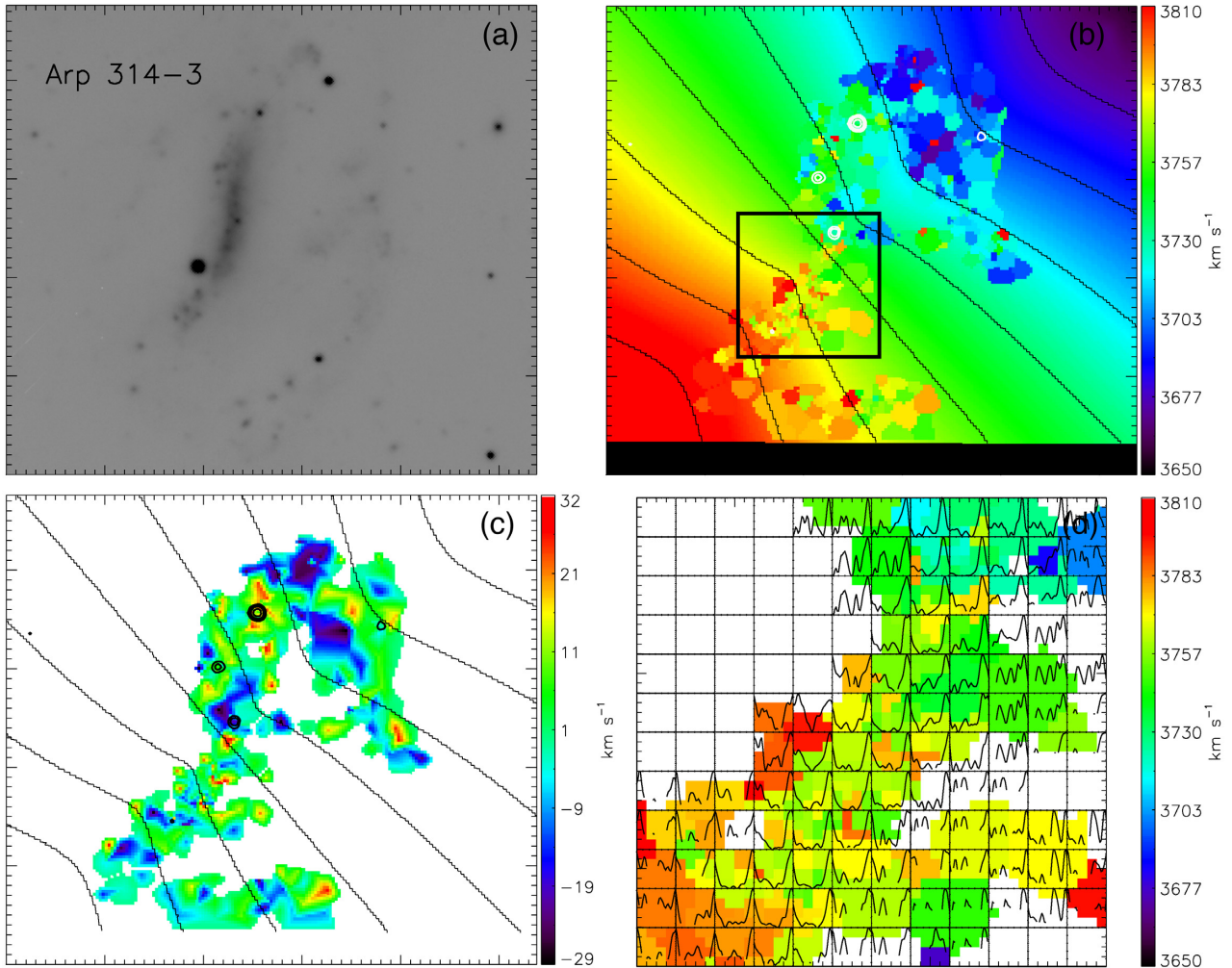


**Figure 7.** Same caption as for Fig. 5, but for Arp 314-3.

Stellar masses are tabulated in Table 4 (column 6), including the galaxy Arp 314-1, given that the stellar mass is mainly derived from the stellar emission, W1, which should not strongly be affected by AGN activity.

Considering the  $M_*$  values, and the SFRs, we estimate the specific SFR (sSFR) for Arp 314-2, value that is listed in the last column of Table 4. Its sSFR shows that Arp 314-2 [ $\log(\text{SFR}_{\text{H}\alpha+22\mu\text{m}}/M_*) = -9.48 \text{ yr}^{-1}$ ] lies in the star-forming sequence in the mass versus sSFR diagram shown by Schiminovich et al. (2007). Considering its mass, this galaxy is actively forming stars, where the gravitational encounter with its companion Arp 314-1 could play a role. Indeed, from Fig. 1 it is evident that a galaxy–galaxy encounter has modified the morphology of Arp 314-2. Finally, we could not compute the sSFR for Arp 314-1 and Arp 314-3.

## 5 DISCUSSION

### 5.1 Gas flows and the flattening of the gas-phase oxygen distribution

Several authors have found that interacting galaxies display flatter metallicity gradients than isolated systems, suggesting that gas flows during interacting events play an important role in the chemical

evolution of these systems (e.g. Kewley et al. 2006, 2010; Rupke, Kewley & Chien 2010b). These gas flows should produce a metal dilution in the central region of interacting galaxies and they may be responsible in triggering a star formation burst. These observational results have been confirmed by simulations (e.g. Rupke et al. 2010a). However, the suggested and expected gas flows are difficult to observe, given the complexity of interacting systems and also due to the lack of large field-of-view high-resolution spectroscopic data. In this sense, a combination of data that allow us to determine metallicity gradients (in large areas) plus a detailed kinematic analysis is essential to understand metallicity gradients in interacting systems. This has motivated us to study the metallicity evolution in a sample of galaxies located in small nearby galaxy groups. For most of these groups, we have high-resolution Fabry–Perot H $\alpha$  spectroscopic data, which are useful to determine the kinematics of these systems.

As part of this project, Torres-Flores et al. (2014a) have studied the metal distribution in the tidal tails of NGC 92, which is the main galaxy of the compact group called Robert’s quartet, and found that NGC 92 displays a flat metallicity distribution along its tidal tail. However, a kinematic analysis on this system did not reveal the existence of gas flow along it. As another part of this project, Torres-Flores et al. (2015) and Alfaro-Cuello et al. (2015) have studied the metal distribution in the merging compact group HCG



## REFERENCES

- Alfaro-Cuello M., Torres-Flores S., Carrasco E. R., Mendes de Oliveira C., de Mello D. F., Amram P., 2015, *MNRAS*, 453, 1355
- Allende Prieto C., Lambert D. L., Asplund M., 2001, *ApJ*, 556, L63
- Amram P., Mendes de Oliveira C., Plana H., Balkowski C., Hernandez O., 2007, *A&A*, 471, 753
- Arp H., 1966, *ApJS*, 14, 1
- Arribas S., Colina L., Bellocchi E., Maiolino R., Villar-Martín M., 2014, *A&A*, 568, A14
- Barrera-Ballesteros J. K. et al., 2015, *A&A*, 579, A45
- Bastian N., Trancho G., Konstantopoulos I. S., Miller B. W., 2009, *ApJ*, 701, 607
- Bell E. F., de Jong R. S., 2001, *ApJ*, 550, 212
- Bresolin F., Kennicutt R. C., Ryan-Weber E., 2012, *ApJ*, 750, 122
- Calzetti D., Armus L., Bohlin R. C., Kinney A. L., Koornneef J., Storchi-Bergmann T., 2000, *ApJ*, 533, 682
- Calzetti D. et al., 2007, *ApJ*, 666, 870
- Cappellari M., Emsellem E., 2004, *PASP*, 116, 138
- Cardelli J. A., Clayton G. C., Mathis J. S., 1989, *ApJ*, 345, 245
- Cluver M. E. et al., 2014, *ApJ*, 782, 90
- Di Matteo P., Combes F., Melchior A. L., Semelin B., 2007, *A&A*, 468, 61
- Di Matteo P., Combes F., Chilingarian I., Melchior A. L., Semelin B., 2008, *Astron. Nachr.*, 329, 952
- Domínguez A. et al., 2013, *ApJ*, 763, 145
- Ellison S. L., Patton D. R., Simard L., McConnachie A. W., 2008, *AJ*, 135, 1877
- Ellison S. L., Mendel J. T., Patton D. R., Scudder J. M., 2013, *MNRAS*, 435, 3627
- Ellison S. L., Patton D. R., Simard L., McConnachie A. W., Baldry I. K., Mendel J. T., 2010, *MNRAS*, 407, 1514
- Epinat B., Amram P., Marcelin M., 2008, *MNRAS*, 390, 466
- Epinat B., Amram P., Balkowski C., Marcelin M., 2010, *MNRAS*, 401, 2113
- Firpo V., Bosch G., Hägele G. F., Morrell N., 2010, *MNRAS*, 406, 1094
- Fitzpatrick E. L., 1999, *PASP*, 111, 63
- Font J. et al., 2011, *ApJ*, 740, L1
- Fujita Y., 2004, *PASJ*, 56, 29
- Gil de Paz A. et al., 2007, *ApJS*, 173, 185
- Hägele G. F., Díaz Á. I., Cardaci M. V., Terlevich E., Terlevich R., 2007, *MNRAS*, 378, 163
- Hernquist L., Quinn P. J., 1989, *ApJ*, 342, 1
- Hodge P., 1993, in Cassinelli J. P., Churchwell E. B., eds, *ASP Conf. Ser. Vol. 35, Massive Stars: Their Lives in the Interstellar Medium*. Astron. Soc. Pac., San Francisco, p. 473
- Hook I. M., Jørgensen I., Allington-Smith J. R., Davies R. L., Metcalfe N., Murowinski R. G., Crampton D., 2004, *PASP*, 116, 425
- Jarrett T. H. et al., 2013, *AJ*, 145, 6
- Kennicutt R. C. Jr, 1998, *ARA&A*, 36, 189
- Kennicutt R. C. Jr, Hodge P. W., 1984, *PASP*, 96, 944
- Kewley L. J., Geller M. J., Barton E. J., 2006, *AJ*, 131, 2004
- Kewley L. J., Rupke D., Zahid H. J., Geller M. J., Barton E. J., 2010, *ApJ*, 721, L48
- Knapen J. H., Cisternas M., Querejeta M., 2015, *MNRAS*, 454, 1742
- Larson R. B., Tinsley B. M., Caldwell C. N., 1980, *ApJ*, 237, 692
- Marino R. A. et al., 2013, *A&A*, 559, A114
- Martin C. L., Kobulnicky H. A., Heckman T. M., 2002, *ApJ*, 574, 663
- Meidt S. E. et al., 2014, *ApJ*, 788, 144
- Melnick J., Tenorio-Tagle G., Terlevich R., 1999, *MNRAS*, 302, 677
- Moreno J., Torrey P., Ellison S. L., Patton D. R., Bluck A. F. L., Bansal G., Hernquist L., 2015, *MNRAS*, 448, 1107
- Mould J. R. et al., 2000, *ApJ*, 529, 786
- Muñoz-Mateos J. C., Gil de Paz A., Boissier S., Zamorano J., Jarrett T., Gallego J., Madore B. F., 2007, *ApJ*, 658, 1006
- Muñoz-Mateos J. C. et al., 2015, *ApJS*, 219, 3
- Nordgren T. E., Chengalur J. N., Salpeter E. E., Terzian Y., 1997, *AJ*, 114, 913
- Olave-Rojas D., Torres-Flores S., Carrasco E. R., Mendes de Oliveira C., de Mello D. F., Scarano S., 2015, *MNRAS*, 453, 2808
- Osterbrock D. E., 1989, *Astrophysics of Gaseous Nebulae and Active Galactic Nuclei*. University Science Books, Mill Valley, CA, p. 422
- Pettini M., Pagel B. E. J., 2004, *MNRAS*, 348, L59
- Querejeta M. et al., 2015, *ApJS*, 219, 5
- Rampazzo R., Plana H., Amram P., Bagarotto S., Boulesteix J., Rosado M., 2005, *MNRAS*, 356, 1177
- Rupke D. S., Veilleux S., Sanders D. B., 2005, *ApJS*, 160, 87
- Rupke D. S. N., Kewley L. J., Barnes J. E., 2010a, *ApJ*, 710, L156
- Rupke D. S. N., Kewley L. J., Chien L.-H., 2010b, *ApJ*, 723, 1255
- Sánchez-Blázquez P. et al., 2006, *MNRAS*, 371, 703
- Scarano S., Jr, Lépine J. R. D., Marcon-Uchida M. M., 2011, *MNRAS*, 412, 1741
- Scarano S., Madsen F. R. H., Roy N., Lépine J. R. D., 2008, *MNRAS*, 386, 963
- Schimionovich D. et al., 2007, *ApJS*, 173, 315
- Scudder J. M., Ellison S. L., Torrey P., Patton D. R., Mendel J. T., 2012, *MNRAS*, 426, 549
- Smith B. J., Struck C., Hancock M., Appleton P. N., Charmandaris V., Reach W. T., 2007, *AJ*, 133, 791
- Torres-Flores S., Scarano S., Mendes de Oliveira C., de Mello D. F., Amram P., Plana H., 2014a, *MNRAS*, 438, 1894
- Torres-Flores S., Amram P., Mendes de Oliveira C., Plana H., Balkowski C., Marcelin M., Olave-Rojas D., 2014b, *MNRAS*, 442, 2188
- Torres-Flores S., Mendes de Oliveira C., Amram P., Alfaro-Cuello M., Carrasco E. R., de Mello D. F., 2015, *ApJ*, 798, L24
- Tremonti C. A. et al., 2004, *ApJ*, 613, 898
- Weilbacher P. M., Duc P.-A., Fritze-v. Alvensleben U., 2003, *A&A*, 397, 545
- Wen X.-Q., Wu H., Zhu Y.-N., Lam M. I., Wu C.-J., Wicker J., Long R. J., Zhao Y.-H., 2014, *MNRAS*, 438, 97
- Wright E. L. et al., 2010, *AJ*, 140, 1868
- Zabludoff A. I., Mulchaey J. S., 1998, *ApJ*, 496, 39
- Zaritsky D., Kennicutt R. C., Jr, Huchra J. P., 1994, *ApJ*, 420, 87

This paper has been typeset from a  $\text{\TeX}/\text{\LaTeX}$  file prepared by the author.